

Surface Structures and Crystal Morphology of ZnS: Computational Study

Said Hamad, Sylvain Cristol,* and C. Richard A. Catlow

Davy Faraday Research Laboratory, The Royal Institution of Great Britain, 21 Albemarle Street, London W1S 4BS, U.K.

Received: June 27, 2002; In Final Form: August 2, 2002

Both cubic and hexagonal phases of ZnS are modeled using interatomic potential based simulations and density functional theory. A new set of potential parameters is derived, showing improved behavior compared with the previous ones. Results obtained with this new potential model show very good agreement with those obtained with density functional theory calculations and with experimental results when available. To calculate crystal morphologies for both phases, we perform an extensive study of the surface energies. In the cubic phase we take into account all the nonpolar surfaces with Miller indexes 0, 1, 2, 3, and 4, and all the polar surfaces with indexes 0, 1, and 2. The nonpolar (110) surface is the most stable surface in this phase and entirely dominates the crystal morphology, which is a dodecahedron showing only the (110) surface and its equivalents. In the hexagonal phase we find that it is necessary to take into account polar surfaces to obtain the crystal morphology, which has a highly anisotropic, cylindrical-like shape, with nonpolar surfaces on the sides and polar surfaces closing the cylinder.

1. Introduction

II–IV semiconductor compounds have been widely studied owing to their electronic properties, among which the most promising is probably the confinement effect that allows the tuning of the electronic energy levels by varying the size of the particles.¹ It is thus of great importance to control the nucleation and growth of this class of compounds. However, the understanding of those processes is limited. Furthermore, the properties of the so-called quantum dots will be strongly dependent on their geometry, which is not always well-known. Surface energies and properties have a great importance in crystal growth, and consequently in nanoparticles sizes and crystal morphologies. Many studies concerning theoretical (mainly tight binding) methods and experimental surface studies of II–VI compound semiconductor have been reported.^{2–4} The main findings are that all the surfaces studied, i.e., (110) of the cubic phase and the (10 $\bar{1}$ 0) and (11 $\bar{2}$ 0) of the hexagonal phase, present the same kind of surface relaxation: anions relax outward from the surface, and cations relax inward. Wang and Duke³ indeed suggested that all the II–VI semiconductor surfaces have similar relaxed geometries. However, one of the limitations of those studies is that only nonpolar surfaces are studied. In contrast, this paper considers polar as well as nonpolar surfaces using computer simulation techniques that have already been shown to be very effective in the prediction of solid state and surface properties and that can be extended to nucleation and growth phenomena.^{5,6}

We focus in this paper on zinc sulfide, which we model using lattice statics simulations based on interatomic potentials. Zinc sulfide has two polymorphs: the most stable sphalerite (cubic) structure and the high-temperature wurtzite (hexagonal) phase. The local structure is the same in both phases with a tetrahedral coordination for both zinc and sulfur. The two phases differ only through the stacking of the atomic planes. Our first requirement is therefore to develop an interatomic potential that can accurately describe both phases. Having developed a satisfactory model, we then proceed with a comprehensive

survey of the surfaces exposed in ZnS crystals, allowing us to predict the morphologies of both phases. The results of the calculation employing interatomic potential are compared with those based on density functional theory, and both are compared with available experimental data, revealing a satisfactory measure of agreement.

2. Methodology

The main approach used in this paper is *lattice statics simulation*, in which we minimize the total energy of the lattice to determine the surface structure, employing interatomic potentials. Moreover, as noted, we have verified some of the surface structures with electronic structure techniques using density functional theory. We used the MARVIN code⁷ for surface calculations with interatomic potentials (IP). Within this approach the surface is modeled by repeating periodically the unit cell in two dimensions. The unit cell is split in two regions (Figure 1). Region 1 contains the surface atoms and the atoms near the surface region. All the atoms in region 1 are allowed to relax. The atoms in region 2 are kept fixed, in the equilibrium positions of the bulk structure, and model the effect of the bulk on the surface.

Two parameters of the calculation must be checked carefully to ensure a correct description of the surface. First, the thickness of region 2 must be large enough for the atoms at the bottom of region 2 to have a negligible interaction with the atoms of the bottom of region 1. Second, the thickness of region 1 must be large enough to ensure that the energy (per surface area unit) is converged. In this study, surface vectors range from 5 to 8 Å and region 1 is made of typically 8 layers (~15 Å) whereas region 2 contains approximately 10 layers (~20 Å). This leads to a total number of atoms of ~150 for a 1 × 1 simulation cell, ~600 for a 2 × 2, and ~1400 for a 3 × 3.

The interactions between the atoms are calculated by the Born model of the solid, with two main contributions to the energy: the long-range interaction, i.e., the electrostatic interaction between the charges of all the ions to which is added a short-range potential. The latter models both the repulsive interactions

* Corresponding author. E-mail: sylvain@ri.ac.uk.

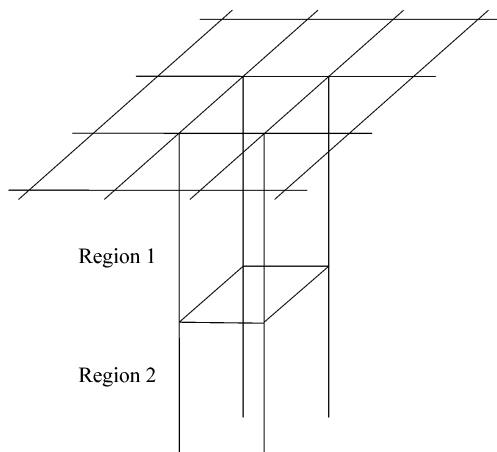


Figure 1. Schematic representation of the unit cell used in the MARVIN code, repeated in two dimensions and split in two regions. Atoms in region 1 are allowed to relax, and atoms in region 2 are kept fixed.

due to the Pauli forces, and the attractive interactions due to the van der Waals dispersion forces. In our case, a mixed Buckingham and Lennard-Jones 9-6 potential models the short-range interaction:

$$V_{ij}^{\text{short}} = A \exp\left(-\frac{r_{ij}}{\rho}\right) + Br_{ij}^{-9} - Cr_{ij}^{-6} \quad (1)$$

where A , B , C , and ρ are fitted parameters.

Due to the semicovalent nature of our material, we also use a three-body potential for the S–Zn–S angle, to take into account the directionality of the covalent bond:

$$V_{ijk} = \frac{1}{2} K_{\text{TB}} (\theta_{ijk} - \theta_0)^2 \quad (2)$$

where θ_0 is the equilibrium angle between S–Zn–S and K_{TB} is a fitted force constant.

Finally, the polarizability of the sulfur anion is introduced through the shell model of Dick and Overhauser.⁸ The charge on the atom is split into a core (carrying the mass of the atom) and a massless shell. The sum of the core charge and the shell charge leads to the total charge of the ion. The core and shell of the same atom interact with a harmonic potential:

$$V_{ij}^{\text{core-shell}} = \frac{1}{2} K r_{ij}^2 \quad (3)$$

where r_{ij} is the core–shell separation and the spring constant, K , is fitted as well as the shell charge.

As the polarizability of the sulfur anion is far greater than that of the zinc cation, a shell model description of the latter ion is not included.

The electrostatic interaction is a long-range interaction and the total electrostatic energy is a conditionally convergent sum. Parry⁹ and Heyes et al.¹⁰ developed a two-dimensional version of the Ewald sum to have a convergent sum with fast convergence, which is the method followed in MARVIN.

The surface energy is a magnitude directly related to the stability of the surfaces. It is the energy necessary to cleave an infinite crystal to create a surface, and for a surface described by the Miller indexes (hkl) it can be calculated as follows:

$$E_S(hkl) = \frac{[E_{\text{region1}}(hkl) - nE_{\text{bulk}}]}{A(hkl)} \quad (4)$$

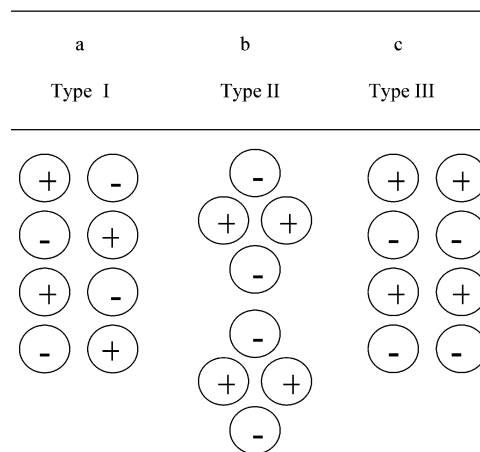


Figure 2. Charge arrangements characteristic of the three different types of surfaces. (a) Type I surface, consisting in a repetition of neutral planes: (b) Type II surface, constructed by a repetition of a neutral stack of planes, each one of which is charged. Depending on where the crystal is cleaved, the surface may be polar or nonpolar. In the figure, the crystal is cleaved showing a nonpolar surface. (c) Type III surface, consisting of a repetition of charged planes that create a dipole, prohibiting cleavage to form a nonpolar surface.

where $E_{\text{region1}}(hkl)$ is the energy of all the atoms modeling the surface block, n is the number of unit cells in region 1, E_{bulk} is the energy per unit cell in the bulk, and $A(hkl)$ is the surface area of the simulation cell.

As shown by Bertaut,¹¹ if the surface presents a dipole perpendicular to the surface direction, the surface energy will diverge due to the generation of a macroscopic field across the crystal. Considering a crystal as a repetition of planes, Tasker¹² made a classification of the surfaces into three types based on the presence or the absence of such dipoles. Type I surfaces (Figure 2a) are constructed by a repetition of neutral planes and cannot present a dipole moment perpendicular to the surface. Type II surfaces (Figure 2b) are constructed by repeating a stack of planes; each stack is charge neutral, but depending on where the crystal is cleaved to expose the surface, the structure may or may not be polar. Type III surfaces (Figure 2c) consist of a repetition of charged planes, with no possibility of cleaving the crystal to have a nonpolar surface. Polar surfaces are unstable, unless the dipole is removed. Several ways are possible to remove this dipole: surface oxidation or reduction, electronic transfer across the crystal,¹³ or geometrical reconstruction. The last method is used in this paper, following the method proposed by Harding.¹⁴

Having computed the surface energies, we can obtain the crystal morphology through Gibbs' criteria,¹⁵ which states that the equilibrium geometry of the crystal should have minimal total surface energy for a given volume. The equilibrium morphology of the crystal is then the one minimizing the following energy:

$$E_{\text{Stotal}} = \sum_{hkl} E_S(hkl) A(hkl) \quad (5)$$

The Dmol³ program^{16,17} has been used for our density functional theory calculations (DFT). We used a double numerical basis set and introduced polarization functions, which proved to be particularly important to obtain a correct description of the sulfur atom yielding the correct lattice parameters for the bulk structures. The Kohn–Sham equations were solved using the gradient-corrected exchange–correlation functional from Perdew et al.^{18,19} Convergence in k -point sampling for Brillouin zone

TABLE 1: Comparison of the Bulk Properties Calculated by the New Interatomic Potential with Experimental Values^a

	expt	IP
sphalerite		
a (Å)	5.409	5.410
C_{11} (10^{11} dyn/cm ²)	10.46	10.51
C_{12} (10^{11} dyn/cm ²)	6.53	6.78
C_{44} (10^{11} dyn/cm ²)	4.61	4.31
ϵ_{stat}	7.9	6.3
ν_1 (cm ⁻¹)	270	260
ν_2 (cm ⁻¹)	350	351
bulk modulus (Gpa)	78	80
wurtzite		
a (Å)	3.85	3.87
c (Å)	6.29	6.10
z_0	0.375	0.384
C_{11} (10^{11} dyn/cm ²)	12.24	12.42
C_{12} (10^{11} dyn/cm ²)	6.01	5.98
C_{13} (10^{11} dyn/cm ²)	4.554	5.80
C_{33} (10^{11} dyn/cm ²)	14.000	11.30
C_{55} (10^{11} dyn/cm ²)	2.864	3.73

^a Properties highlighted in bold have been used in the fitting procedure.

integration was checked for each surface using a Monkhorst–Pack²⁰ mesh centered on the Γ point. The converged k -point grids are found to be $5 \times 5 \times 1$ for the (110) surface, $5 \times 5 \times 1$ for (1120), and $5 \times 7 \times 1$ for the (1010) surface. Two-dimensional periodicity is not implemented in Dmol³. We thus used the slab approach to model the surfaces with a three-dimensional periodic supercell. In plane-wave based techniques, the vacuum gap between the slabs is normally limited because the computation time scales not only with the number of atoms but also with the volume of the simulation cell, as a larger volume requires more plane waves. Fortunately, the localized basis set used in Dmol³ allow the separation between the slabs to be as large as necessary to avoid spurious interaction between slabs. Simulation cells up to 40 Å in the direction perpendicular to the surface have been used, with the surfaces modeled by 8 layers (32 atoms). The upper four layers are allowed to relax and the bottom four are kept fixed in the optimized bulk geometry.

3. Results and Discussion

3.1. Derivation of the New Potential. The previously published set of atomistic potentials²¹ gives acceptable structural parameters and the elastic constant for the cubic phase but does not describe its vibrational properties adequately. Furthermore, it uses a shell model on the zinc atom with a very low spring constant, which makes it unstable during molecular dynamics simulations. Although molecular dynamics will not be used in this paper, we plan to use this technique extensively in further studies of the nucleation of ZnS. A new set of parameters for the description of both phases of zinc sulfide was clearly necessary, which to achieve, we undertook parameter fitting with the GULP²² code using structural parameters²³ and elastic constants²⁴ for both phases and Γ -point phonon frequencies for sphalerite.²⁵ Overall, 10 experimental values have been used to derive 9 parameters. The other experimental values were checked afterwards. We checked that the lattice energy is converged for a cutoff distance of 15 Å. This quite high value is needed because of the large C ($1/r^6$) parameter in the S–S Buckingham potential. Table 1 shows the comparison between calculated and experimental values for both polymorphs. The final parameters are compiled in Table 2. The agreement between experimental and computed values is very good,

TABLE 2: Potential Parameters Derived in This Study^a

general potential	A (eV)	ρ (Å)	B (eV·Å ⁹)	C (eV·Å ⁶)
Zn–S	213.20	0.475	664.35	10.54
S–S	11413.09	0.153	0.0	129.18
spring potential			K (eV·Å ⁻²)	
S core–S shell			27.690	
three-body potential		θ_o (deg)	K_{TB} (eV·rad ⁻²)	
Zn core–S shell – S shell		109.47	0.778	
ion charges			charge (e)	
Zn core			2.0000	
S core			1.357	
S shell			−3.357	

^a A cutoff distance of 15 Å has been used for all short-range potentials.

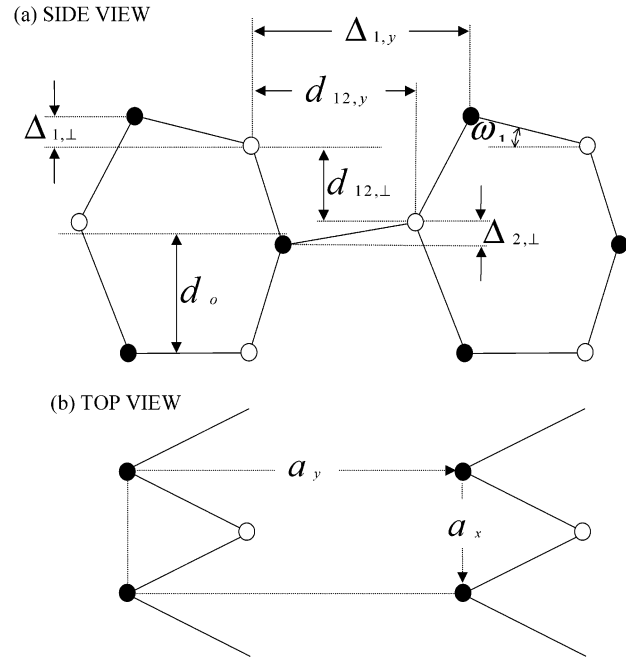


Figure 3. Side and top views of the relaxed surface geometry for the (110) surface of cubic ZnS. Full circles denote sulfur atoms, and open circles, zinc atoms.

although we note that the parameter fitting was weighted toward reproduction of the cubic structure, as it is the most important polymorph. We also checked that our parameters give reliable geometries for small clusters— $(\text{ZnS})_n$, $n = 2-7$ —as computed by DFT calculations. This verification has been made by comparing geometries (bond distances within 0.1 Å and bond angles within 5°) obtained from the same starting geometry. This interatomic potential should then be transferable to surfaces and clusters although it is fitted on bulk properties.

3.2. Surface Geometries and Surface Energies. **3.2.1. Cubic Phase.** To predict the morphology of a crystal, it is necessary to study several surfaces. We have studied all the nonpolar surfaces with Miller indexes 0, 1, 2, 3, and 4, and all the polar surfaces with indexes 0, 1, and 2. A general feature is that the higher the Miller index of a surface, the higher its surface area, and consequently the corresponding surface will be less likely to appear in the morphology (see eq 5). Hence, the condition of only showing faces with 0, 1, 2, 3, and 4 Miller indexes is not very restrictive. The (110) surface is the most important in zinc blende II–VI semiconductors (Figure 3). We studied this surface within two approaches: lattice statics and DFT calcula-

TABLE 3: Geometric Parameters Showing Atomic Relaxation Displacements for the (110) Surface of Cubic ZnS, As Defined in Figure 3^a

	IP	DFT	expt
a_x	3.825	3.868	3.825
a_y	5.410	5.470	5.409
$\Delta_{1,\perp}$	0.354	0.574	0.59
$\Delta_{1,y}$	4.231	4.381	4.296
$d_{12,y}$	2.947	3.120	3.149
$d_{12,\perp}$	1.593	1.443	1.403
$\Delta_{2,\perp}$	0.065	0.119	0.000
d_o	1.913	1.903	1.912
ω_1	16.72	27.76	28.0

^a All data are in Å except ω_1 , which is in degrees. Experimental data are collected from ref 26.

TABLE 4: Relaxed Surface Energies of Differently Reconstructed Polar Surfaces of Cubic ZnS: (100) S-terminated, (100) Zn-terminated, (111) Zn-terminated and (111) S-terminated^a

surface				surface energy (J/m ²)
100	S	Point	1 × 1	1.30
100	S	Point	2 × 2	1.30
100	S	Point	3 × 3	1.30
100	S	Linear	2 × 2	2.02
100	S	Terraced	2 × 2	1.49
100	S	Terraced	3 × 3	1.68
100	Zn	Point	1 × 1	1.12
100	Zn	Point	2 × 2	1.12
100	Zn	Point	3 × 3	1.12
100	Zn	Linear	2 × 2	1.47
100	Zn	Terraced	2 × 2	1.16
100	Zn	Terraced	3 × 3	1.44
111	Zn	Point	1 × 1	0.87
111	Zn	Point	2 × 2	0.87
111	Zn	Point	3 × 3	0.87
111	Zn	Linear	2 × 2	1.41
111	Zn	Terraced	2 × 2	1.14
111	Zn	Terraced	3 × 3	1.83
$\bar{1}\bar{1}\bar{1}$	S	Point	1 × 1	1.01
$\bar{1}\bar{1}\bar{1}$	S	Point	2 × 2	1.01
$\bar{1}\bar{1}\bar{1}$	S	Point	3 × 3	1.01
$\bar{1}\bar{1}\bar{1}$	S	Linear	2 × 2	does not converge
$\bar{1}\bar{1}\bar{1}$	S	Terraced	2 × 2	1.14
$\bar{1}\bar{1}\bar{1}$	S	Terraced	3 × 3	1.29

^a The first column in the surface description shows the surface, the second the atom with which it is terminated, the third the kind of reconstruction (see text) and the fourth the number of minimum unit cells contained in our simulation cell.

tions. Both of them give the correct relaxation behavior, anions displacing outward from the surface and cations moving inward. As shown in Table 3, the distance between S and Zn of the first layer in the direction perpendicular to the surface ($\Delta_{1,\perp}$) is 0.35 Å when computed with lattice statics. The DFT result of 0.57 Å is closer to the experimental²⁶ value of 0.59 Å. In the second layer this perpendicular relaxation between S and Zn has been experimentally²⁶ measured as close to zero, whereas the DFT calculations calculate 0.12 Å for this distance. In this case, the interatomic potential based result, 0.06 Å, is in better agreement with experiment. Lattice statics results are thus comparable in accuracy with DFT and we get an acceptable agreement with experimental results.

All the other surfaces in the cubic phase have been treated only with lattice statics calculations. Polar surfaces have been reconstructed geometrically by translating some atoms from the top layer to the bottom of the simulation cell to quench the surface dipole. Physically, this procedure is equivalent to the creation of surface defects. There is, however, no unique way

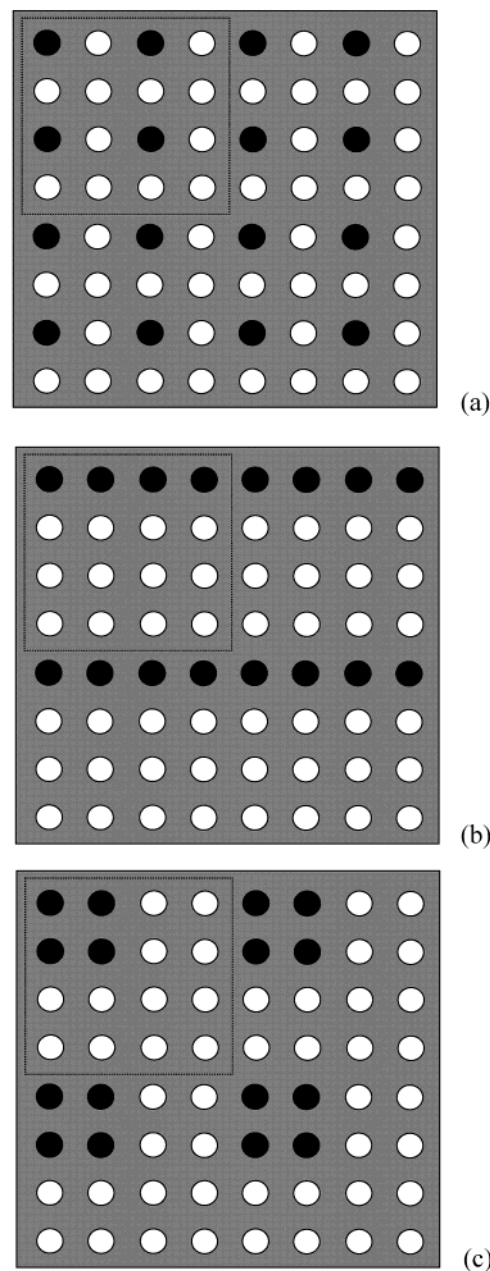


Figure 4. Schematic representation of a surface (top view): (a) “point” reconstruction; (b) “linear” reconstruction; (c) “terraced” reconstruction. White circles represent surface atoms, and black atoms represent the vacancies created to remove the dipole. The repeated unit cell is surrounded by a dashed square. In this example dipole removal is achieved by translating 1 out of 4 surface atoms. (See text.)

of creating these defects, and various arrangements of defect have been studied, to check which is the most stable reconstruction. We studied this effect on three polar surfaces, (100), (111), and $\bar{1}\bar{1}\bar{1}$, with three different reconstructions for each one. The first type of reconstruction is denoted “point” and is characterized by the largest possible separation between the defects. The goal is to be as close as possible to noninteracting local defects. The second type of reconstruction is denoted “linear”, because defects are created following a linear arrangement on the surface. The third type of reconstruction is referred to as “terraced”, as all the defects are localized in the same area, forming a terraced surface. Surface energies of the different reconstructions studied are shown in Table 4, and Figure 4 shows the three kinds of reconstruction. For symmetry reasons, the surface energy for “point” reconstruction does not change with an increase of the

TABLE 5: Surface Energies for Polar and Nonpolar Surfaces of Cubic ZnS^a

surface		surface energy (J/m ²)
110		0.53
431		0.78
431		0.84
111	Zn	0.87
321		0.95
111	S	1.01
221	Zn	1.01
221	S	1.06
210	S	1.08
100	Zn	1.12
210	Zn	1.14
211		1.17
321		1.19
310		1.27
211		1.28
100	S	1.30

^a S and Zn denote the atom with which the polar surface is terminated.

simulation cell: a change in the size of the simulation cell does not affect the structure of the surface. The behavior of the “terraced” reconstruction is, in contrast, divergent. An increase of the size of the simulation cell leading to larger terraces induces an increase in the surface energy. Linear reconstruction can only be obtained with a 2×2 surface because of the stoichiometry needed for the reconstruction.

The lowest surface energy is always obtained with “point” reconstruction for which the surface relaxation is small. On the other hand, linear and terraced defect arrangements strongly distort the surfaces, inducing strong geometric relaxation and a high surface energy. The main conclusion is that, as far as geometrical reconstruction is considered, the most stable way of removing a dipole is by creating point defects with the maximum separation on the surface. Such models will therefore be used for all polar surfaces.

The surface energies of all the surfaces modeled for the cubic phase ZnS surfaces are summarized in Table 5, where results on polar and nonpolar surfaces are shown. The most stable surface is (110), with a surface energy of 0.53 J/m², in good agreement with the value obtained from DFT calculations, 0.46 J/m². The next most stable surfaces are the nonpolar (431) and ($\bar{4}31$), 0.78 and 0.83 J/m², respectively, followed by the (111) polar surface, Zn terminated, 0.87 J/m². The higher stability of the (110) surface, compared with any other polar or nonpolar surfaces, has also been observed experimentally,^{27,28} in measurements on thin film layers of ZnS.

It is interesting to note that surface relaxation is not much larger on the polar than on the nonpolar surfaces. Taking the Zn–S distance as a measure of the relaxation, we found that in the nonrelaxed surfaces the value is 2.34 Å, whereas in the relaxed surfaces it is measured between 2.18 and 2.40 Å, for both polar and nonpolar surfaces.

Figure 5 shows the predicted crystal morphology according to our calculations. Although many surfaces are taken into account, only the (110) surface is present in the morphology because of its much higher stability; the resulting shape is a dodecahedron, which is very isotropic.

3.2.2. Hexagonal Phase. The hexagonal phase of ZnS has also been studied with lattice statics and with DFT calculations. Figures 6 and 7 show the (10 $\bar{1}0$) and the (11 $\bar{2}0$) surfaces that have been modeled with both techniques. There are no experimental results available for these surfaces of ZnS, although they have previously been studied theoretically.²⁹ These surfaces

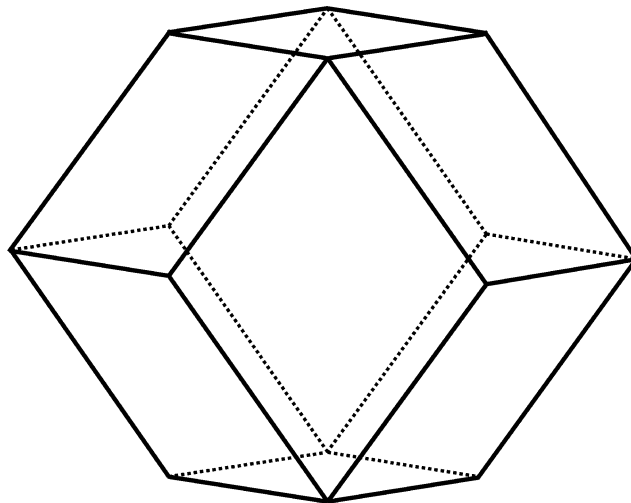


Figure 5. Calculated morphology of the cubic phase of ZnS, obtained by using relaxed surface energies. The only surface to appear is the (110).

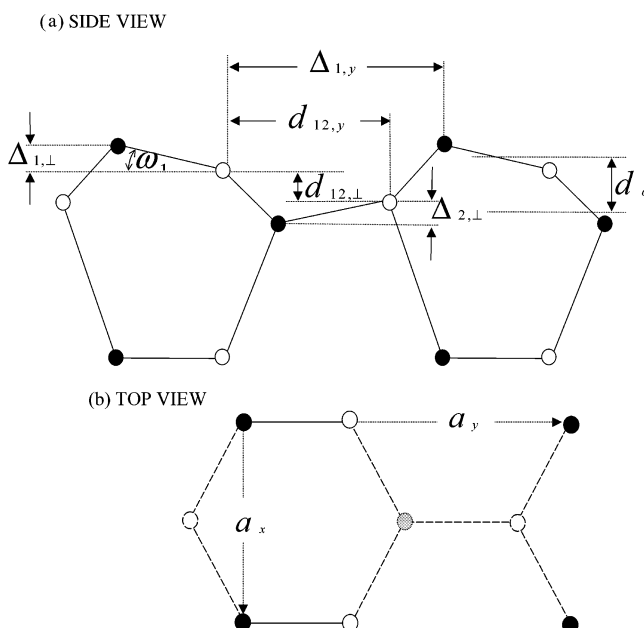


Figure 6. Side and top views of the relaxed surface geometry for the (10 $\bar{1}0$) surface of hexagonal ZnS. Full circles denote sulfur atoms, and open circles, zinc atoms. The top view also shows hatched circles and dashed open circles, representing sulfur and zinc atoms of the second layer, respectively.

have also been widely studied for other II–VI semiconductors^{3,4} and III–V semiconductors.³⁰ Here we also report the first study of the nonpolar (12 $\bar{3}0$) surface and two polar surfaces of wurtzite. Relaxed geometries are reported in Tables 6 and 7, comparing DFT and interatomic potential based results for (10 $\bar{1}0$) and (10 $\bar{2}0$) surfaces, respectively.

As in the cubic phase, the main characteristic of the relaxed surfaces is the displacement of the sulfur atoms outward from and of the zinc atoms toward the surface. In the (110) surface of the sphalerite polymorph, the perpendicular relaxation displacement, $\Delta_{1,\perp}$, was higher for DFT than for lattice statics results. The same trend is found for (11 $\bar{2}0$) and (10 $\bar{1}0$).

Surface energies of (11 $\bar{2}0$) and (10 $\bar{1}0$) surfaces calculated with the DFT calculations are 0.35 and 0.33 J/m², respectively, whereas lattice statics results are 0.49 and 0.52 J/m², respectively. The surface energies are therefore significantly different,

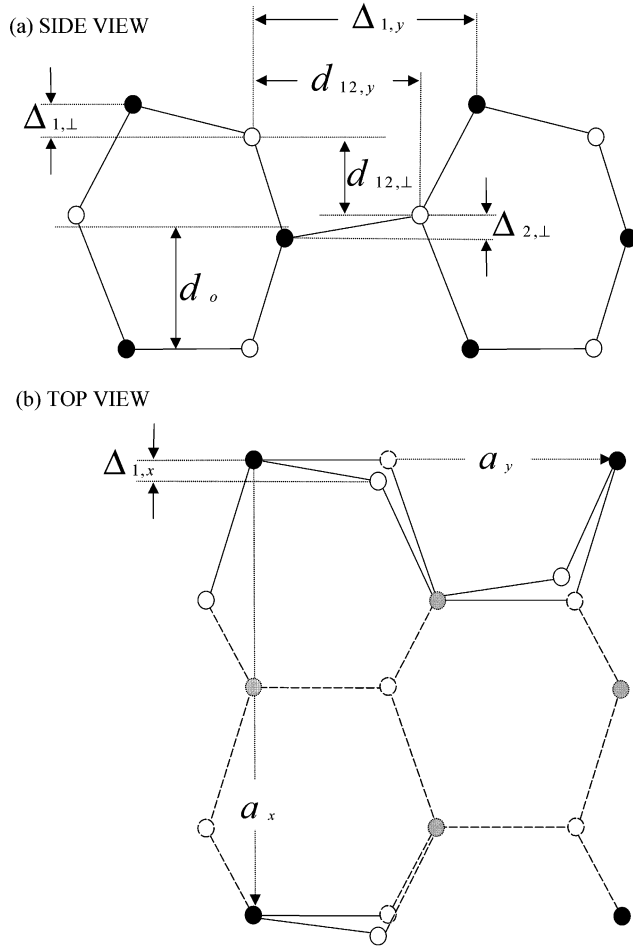


Figure 7. Side and top views of the relaxed surface geometry for the (1120) surface of hexagonal ZnS. Full circles denote sulfur atoms, open circles zinc atoms. The top view also shows hatched circles and dashed open circles, representing sulfur and zinc atoms of the second layer, respectively.

TABLE 6: Geometric Parameters Showing Atomic Relaxation Displacements for the (1010) Surface of Hexagonal ZnS, As Defined in Figure 6^a

	IP	DFT
a_x	3.878	3.871
a_y	6.091	6.332
$\Delta_{1,\perp}$	0.421	0.671
$\Delta_{1,y}$	3.870	4.196
$d_{12,y}$	3.288	3.565
$d_{12,\perp}$	0.711	0.501
$\Delta_{2,\perp}$	0.114	0.120
d_o	1.120	1.100
ω_1	10.8	17.4

^a All data are in Å except ω_1 , which is in degrees.

but both sets of calculations predict that both surfaces have almost the same energy.

The other surfaces, the nonpolar (12 $\bar{3}$ 0) and the two polar surfaces (0001) and (000 $\bar{1}$), have been studied with the interatomic potential method. As we found with the polar surfaces in the cubic phase, the most favorable way of removing the dipole of the surface by geometrical reconstruction is the “point” reconstruction. We therefore used this technique for surface reconstruction of the wurtzite phase. Surface energies of all the studied surfaces of hexagonal ZnS are reported in Table 8. We find that all of the three nonpolar surfaces have almost the same surface energies, which are much lower than

TABLE 7: Geometric Parameters Showing Atomic Relaxation Displacements for the (1120) Surface of Hexagonal ZnS, As Defined in Figure 7^a

	IP	DFT
a_x	6.717	6.705
a_y	6.091	6.332
$\Delta_{1,\perp}$	0.363	0.566
$\Delta_{1,y}$	4.613	4.384
$d_{12,y}$	3.575	3.704
$d_{12,\perp}$	1.617	1.408
$\Delta_{2,\perp}$	0.065	0.100
d_o	1.903	1.955
$\Delta_{1,x}$	0.282	0.425

^a All data are in Å.

TABLE 8: Surface Energies for Polar and Nonpolar Surfaces of Hexagonal ZnS^a

surface	surface energy (J/m ²)
11 $\bar{2}$ 0	0.49
10 $\bar{1}$ 0	0.52
12 $\bar{3}$ 0	0.52
0001	Zn 0.90
000 $\bar{1}$	S 0.91

^a S and Zn denote the atom in which the polar surface is terminated.

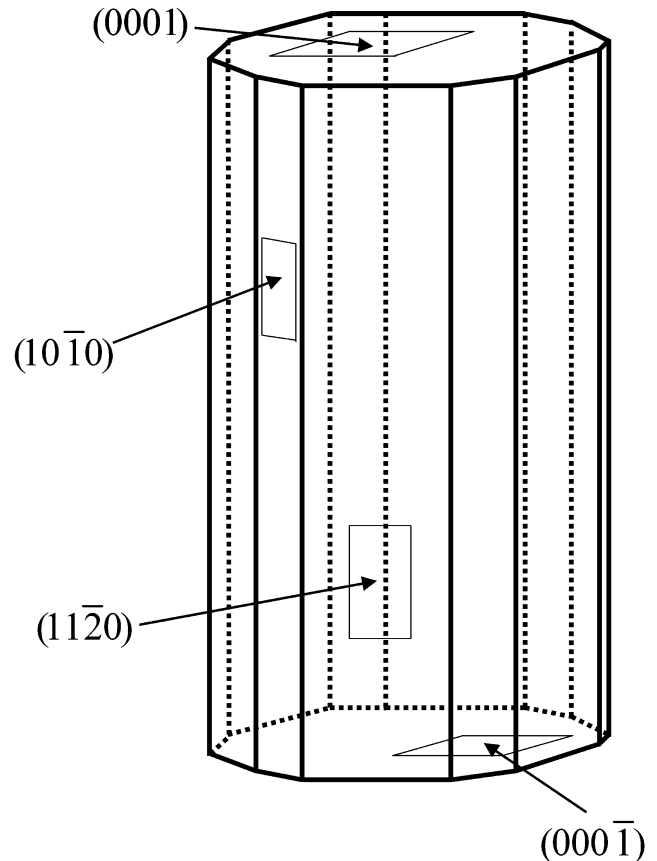


Figure 8. Calculated morphology of the hexagonal phase of ZnS, obtained using relaxed surface energies. The indexes of the surfaces exposed are also shown.

the surface energies of the polar surfaces, and that the energies of the (0001) and (000 $\bar{1}$) surfaces are very similar. Due to its high surface area, the (12 $\bar{3}$ 0) surface does not appear in the calculated crystal morphology of hexagonal ZnS (Figure 8), even though it has almost the same surface energy as the other two nonpolar surfaces. The resulting morphology has a cylindrical-

like shape, which is highly anisotropic, with a large nonpolar area exposing the (11 $\bar{2}$ 0) and (10 $\bar{1}$ 0) surfaces and small areas closing the cylinder exposing the polar (0001) and (000 $\bar{1}$) surfaces.

4. Summary

We have derived a new set of potential parameters, which is able to model both phases of ZnS, cubic and hexagonal, and which enables us to undertake a general study of the surfaces of ZnS. Results obtained from IP calculations are in good agreement with experiment, when available, and with those obtained from DFT calculations. This general study of surface stability has allowed us to predict crystal morphologies for both phases. The most stable surface in the cubic phase of ZnS is the nonpolar (110), followed by the nonpolar (4 $\bar{3}$ 1) and (431) and by the polar (111) surface. The difference in surface energy between the (110) and the other surfaces is large enough to result in this surface dominating the crystal morphology. In the hexagonal phase of ZnS there are three nonpolar surfaces ((11 $\bar{2}$ 0), (10 $\bar{1}$ 0), and (12 $\bar{3}$ 0)), having almost the same energy, but the high surface area of (12 $\bar{3}$ 0) precludes its presence in the crystal morphology. High-energy polar surfaces (0001) and (000 $\bar{1}$) also appear in the predicted morphology, with the morphologies of the two polymorphs being very different. Sphalerite will have isotropic dodecahedral crystals, whereas wurtzite will have cylindrical crystals. These differences could be significant for the electronic and structural properties of semiconductor quantum dots and nanocrystallites, as different geometries might induce different electrical and optical properties for very small structures.

Acknowledgment. We thank the EU-NUCLEUS project for funding and Drs. A. A. Sokol and S. A. French for fruitful discussions.

References and Notes

- (1) Weller, H. *Adv. Mater.* **1993**, 5, 88.
- (2) Duke, C. B. *J. Vac. Sci. Technol. B* **1983**, 1, 732.
- (3) Duke, C. B.; Wang, Y. R. *J. Vac. Sci. Technol. A* **1989**, 7, 2035.
- (4) Rantala, T. T.; Rantala, T. S.; Lantto, V.; Vaara, J. *Surf. Sci.* **1996**, 352–354, 77.
- (5) Sayle, D. C.; Catlow, C. R. A.; Harding, J. H.; Healy, M. J. F.; Maicaneanu, S. A.; Parker, S. C.; Slater, B.; Watson, G. W. *J. Mater. Chem.* **2000**, 10, 1315.
- (6) Catlow, C. R. A.; Coombes, D. S.; Lewis, D. W.; Pereira, J. C. G. *Chem. Mater.* **1998**, 10, 3249.
- (7) Gay, D. H.; Rohl, A. L. *J. Chem. Soc., Faraday Trans.* **1995**, 91, 925.
- (8) Dick, B. G.; Overhauser, A. W. *Phys. Rev.* **1958**, 112, 90.
- (9) Parry, D. E. *Surf. Sci.* **1976**, 54, 195.
- (10) Heyes, D. M.; Barber, M.; Clarke, J. H. R. *J. Chem. Soc., Faraday Trans.* **1997**, 73, 1485.
- (11) Bertaut, F. *Compt. Rend. Acad. Sci. (Paris)* **1958**, 246, 3447.
- (12) Tasker, P. W. *J. Phys. C: Solid State Phys.* **1979**, 12, 4977.
- (13) Wander, A.; Schedin, F.; Steadman, P.; Norris, A.; McGrath, R.; Turner, T. S.; Thornton, G.; Harrison, N. M. *Phys. Rev. Lett.* **2001**, 86, 2811.
- (14) Harding, J. H. *Surf. Sci.* **1999**, 442, 87.
- (15) Gibbs, J. W. *Collected Works*; Longman: New York, 1928.
- (16) Delley, B. *J. Chem. Phys.* **1990**, 92, 508. Dmol³ is available from Accelrys in the Cerius² program suite.
- (17) Delley, B. *J. Chem. Phys.* **2000**, 113, 7756.
- (18) Perdew, J. P.; Chevary, J. A.; Vosko, S. H.; Jackson, K. A.; Pederson, M. R.; Singh, D. J.; Fiolhais, C. *Phys. Rev. B* **1992**, 46, 6671.
- (19) Perdew, J. P.; Wang, Y. *Phys. Rev. B* **1992**, 45, 13244.
- (20) Monkhorst, H. J.; Pack, J. D. *Phys. Rev. B* **1976**, 13, 5188.
- (21) Wright, K.; Jackson, R. A. *J. Mater. Chem.* **1995**, 5, 2037.
- (22) Gale, J. D. *J. Chem. Soc., Faraday Trans.* **1997**, 93, 629.
- (23) Wyckoff, R. W. G. *Crystal Structures*, 2nd ed.; Interscience Publishers: New York, 1967; Vol. 2.
- (24) Lide, D. L. *Handbook of Chemistry and Physics*, 80th ed.; CRC Press: Boca Raton, FL, 1999–2000.
- (25) Bilz, H.; Kress, W. *Phonons dispersion relations in Insulator*; Springer-Verlag: New York, 1979.
- (26) Duke, C. B.; Paton, A.; Kahn, A. *J. Vac. Sci. Technol. A* **1984**, 2, 515.
- (27) Sasakura, H.; Kobayashi, H.; Tanaka, S.; Mita, J.; Tanaka, T.; Nakayama, H. *J. Appl. Phys.* **1981**, 52, 6901.
- (28) Hirabayashi, K.; Kogure, O. *Jpn. J. Appl. Phys.* **1985**, 24, 1484.
- (29) Wang, Y. R.; Duke, C. B. *Phys. Rev. B* **1987**, 36, 2763.
- (30) Mailhot, C.; Duke, C. B.; Chadi, D. J. *Surf. Sci.* **1985**, 149, 366.